

4.2.4.3 CGS Data Analysis

Figures 4.20 and 4.21 present the experimental and theoretical wrapped and unwrapped vertical shearing CGS data from the pure $E_x\hat{i}$ and pure $E_y\hat{j}$ inputs, respectively. The experimental and theoretical wrapped data show similar lobe structures and fringe density, though the experimental data seems to be slightly elongated behind the crack along the vertical shearing direction as explained in Section 4.2.4.1 about the finite shearing distance. Figure 4.20(e) shows a map of the theoretical amplitude $I_c^{Ex} = I_c^{Ey}$, which modulates the $\cos(\varphi_{sum} \pm \varphi_{\alpha d})$ interference term of the intensity expressions in Equations (2.22) and (2.23); the $\arctan()$ formula in Equation (2.21) does not hold for $I_c^{Ex} = I_c^{Ey} = 0$, so those points are likely places for poor fringe quality. In this case, only small regions near the crack tip have $I_c^{Ex} = I_c^{Ey}$ values close to zero; since these points are collected together and do not form a boundary of low-quality data points across which the unwrapping program cannot pass information, the unwrapping algorithm can confine any error to those points.

Figure 4.22 shows the experimental and theoretical wrapped and unwrapped vertical shearing CGS data from the circularly polarized electric field input from the $\lambda/4$ polarization method, the φ_{sum} phase determined from $(\varphi^{Ex} + \varphi^{Ey})/2$, and the $\cos(\varphi_{diff})$ field that modulates the phase from the $\lambda/4$ polarization method, as explained in Section 2.2.3.2. The experimental and theoretical wrapped φ_{sum} from the circularly polarized electric field input data in Figures 4.22(a) and 4.22(b) have similar fringe density and shape, though the lobes behind the crack tip of the experimental data are slightly larger than the theoretical. The experimental fringes have slight errors in a four-leaf clover pattern around the crack tip near where $\cos(\varphi_{diff})$ is close to zero. As expected, data near $\cos(\varphi_{diff}) = 0$ is prone to higher error since the $\arctan()$ function for φ_{sum} in Equation (2.25) is indeterminate at $\cos(\varphi_{diff}) = 0$ and since these locations are where the misalignment of the first $\lambda/4$ plate can affect the CGS data, as discussed in Section 3.2.2. Since Homalite-100 has a small value for the photoelasticity-related constant $g = -0.0844$, which is related to the magnitude of φ_{diff} as defined in Section 2.2.2.2, the effect of the φ_{diff} phase is generally confined to very close to the crack tip even for this case with significant K_I loading; many of these errors are masked by the user-defined crack tip mask, and therefore do not have large influence on the data. The unwrapped phase in

Figure 4.22(c) and the φ_{sum} phase determined from $(\varphi^{Ex} + \varphi^{Ey})/2$ in Figure 4.22(e) are comparable; the experimental fields are able to capture the theoretical change in phase globally except that the negative phase lobes are slightly further back from the crack tip than in the theoretical fields. Since the $\cos(\varphi_{diff})$ field is fairly uniform, the φ_{sum} from the circularly polarized electric field input has few unwrapping errors and is thus a good measure for the derivative of stress, implying that the only the single set of four phase-shifted images are required for Homalite-100 in this configuration.

In Figures 4.23 and 4.24, the experimental and theoretical wrapped and unwrapped horizontal shearing CGS data from the pure $E_x\hat{i}$ and pure $E_y\hat{j}$ inputs have similar fringe density and shape, though in the experimental data the lobes ahead of the crack appear larger, and the lobes along the crack appear smaller than in the theoretical data. The theoretical amplitude $I_c^{Ex} = I_c^{Ey}$ in Figure 4.25(f) is uniform over the field of view except just in front of the crack, which goes to zero; this small area is masked to prevent unwrapping problems due to the poor fringe quality where the $\arctan()$ formula for φ^{Ex} and φ^{Ey} is indeterminate. The experimental and theoretical wrapped and unwrapped φ_{sum} data from the circularly polarized electric field input shown in Figure 4.25 again compare well but with smaller lobes along the crack in the experimental data. The φ_{sum} fields from the circularly polarized electric field input and from $(\varphi^{Ex} + \varphi^{Ey})/2$ in Figures 4.25(c) and 4.25(e), respectively, are nearly identical and nearly match the theoretical phase in Figure 4.25(d), except on either side of the crack where the phase is rather large theoretically. Since $\cos(\varphi_{diff})$ for the horizontal shearing direction is only close to zero just in front of the crack, and the wrapped phase is easily masked there to reduce unwrapping errors, the φ_{sum} data from the circularly polarized electric field input gives as good comparison to the theoretical phase as the φ_{sum} data from $(\varphi^{Ex} + \varphi^{Ey})/2$. Like the vertical shearing, the horizontal shearing CGS for Homalite-100 in this configuration only requires one set of phase-shifted images to determine φ_{sum} .

From the phase data from the pure $E_x\hat{i}$ and pure $E_y\hat{j}$ inputs, Figure 4.26 shows the secondary phases $\varphi_{\alpha d}$ from Equations (2.22) and (2.23) for the vertical and horizontal shearing directions. The experimental $\varphi_{\alpha d}$ for the horizontal direction compares extremely well with the theoretical phase, while the experimental $\varphi_{\alpha d}$ for the vertical direction does not compare as well. The rear lobes of the

vertical $\varphi_{\alpha d}$ are larger and further from the crack in the experimental data than in the theoretical data; the distance that the rear lobes are behind the predicted location is about half of the shearing distance $d_{shear} = 225 \mu\text{m}$. A larger shearing distance increases the fringe density of the images, which improves the measurement for lower-stress regions, but also weakens the approximation of the phase relating to a derivative of stress. Therefore, a careful balance of large enough fringe density with a small enough shearing distance must be struck for quality data. In this case, the errors are localized to the crack tip region of approximately $r < d_{shear}$, most of which is lost due to caustic shadows anyway. This CGS data shows that this method can well approximate the expected phase to within a small distance from the crack tip.

Figure 4.27 shows the x and y derivatives of $\sigma_1 + \sigma_2$ maps and the integrated $\sigma_1 + \sigma_2 + c_i$ map, where c_i is the constant of integration that is determined by a traction-free boundary condition along the crack. Calculated from Equation (2.26), the x and y derivatives of $\sigma_1 + \sigma_2$ come from the vertical and horizontal shearing directions, respectively, for this specimen coordinate system. The integrated $\sigma_1 + \sigma_2 + c_i$ has good symmetry across the crack, though the frontal lobe is slightly skewed to the $-\theta$ direction due to the Mode II loading component.

The initial assumption for using CGS to determine derivatives of the principal stress sum is that the shearing distance is small enough to approximate a finite difference as a first derivative. Bruck and Rosakis (1992, 1993) considered the accuracy of this assumption for CGS in fracture mechanics applications. They calculated the error of this assumption for a K_I -dominant field for both shearing directions around a loaded crack, using the following expression for the x direction (with an equivalent expression for the y direction shear):

$$\epsilon = 1 - \frac{\frac{\partial(\sigma_1(x, y) + \sigma_2(x, y))}{\partial x}}{\left[\frac{(\sigma_1(x + \frac{d_{shear}}{2}, y) + \sigma_2(x + \frac{d_{shear}}{2}, y) - \sigma_1(x - \frac{d_{shear}}{2}, y) - \sigma_2(x - \frac{d_{shear}}{2}, y))}{d_{shear}} \right]}. \quad (4.7)$$

If the loading condition only has a K_I component, as was the only case considered by Bruck and Rosakis (1992, 1993), then the error field plots for the vertical and horizontal shearing directions for the $4.6 \text{ mm} \times 4.6 \text{ mm}$ field of view and lateral shearing distance of $d_{shear} = 225 \mu\text{m}$ are given

in Figure 4.28. These plots indicate regions with error less than 1%, 1%–5%, and greater than 5%, showing symmetry across the crack plane. The regions with greater than 5% error are concentrated around the crack. Since these plots only include a K_I component, then the value of K_I does not affect the error calculation in Equation (4.7) for a given d_{shear} ; therefore, these plots hold for any K_I -dominant field with pure K_I loading.

Given mixed-mode loading conditions, the actual values of K_I and K_{II} play a role in the error calculated with Equation (4.7). For this case where $K_I = 0.514 \text{ MPa}\sqrt{\text{m}}$ and $K_{II} = 4.4 \text{ kPa}\sqrt{\text{m}}$, the error plots for both shearing directions in Figure 4.29 show different behavior than for the K_I -only error plots, where the symmetry across the crack plane is lost, the error in the horizontal shearing direction is very similar to the K_I -only case, and the error in the vertical shearing direction is larger behind the crack with more area with greater than 1% error. These plots indicate why the experimental vertical shearing data appears to be different than the theoretical data behind the crack in Figure 4.22. This error analysis shows the potential regions of higher error in the $\sigma_1 + \sigma_2$, such as behind the crack and close to the crack tip, which may give rise to higher error in the separated stresses in those regions. Fortunately, Figure 4.29 indicates that the majority of the field should have less than 5% error (indicated by the yellow and green regions), so the CGS data may confidently be used to determine the derivative of stress in a global sense.

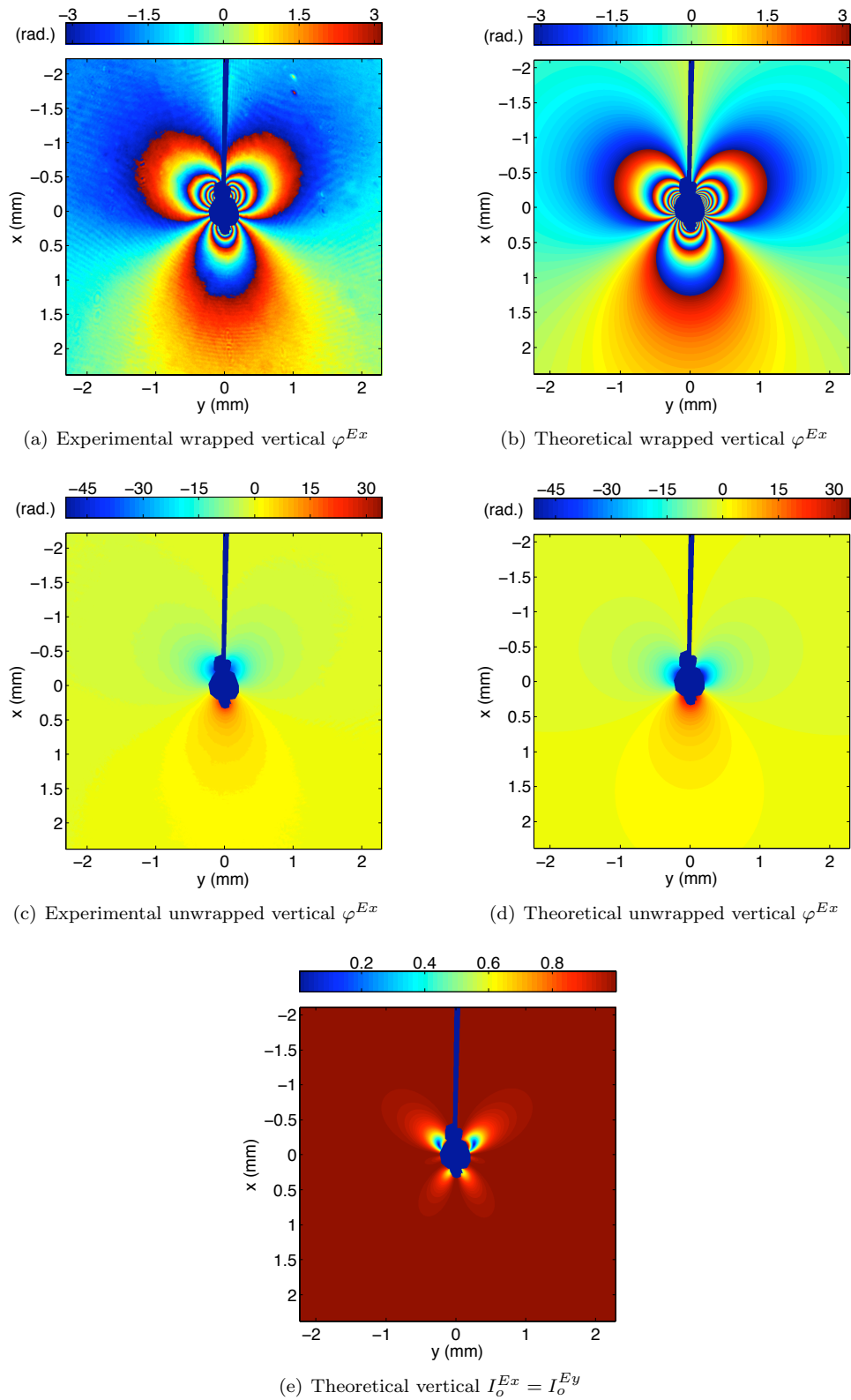


Figure 4.20: Experimental and theoretical φ^{Ex} data for vertical CGS for specimen HomC1 for $K_I = 0.514 \text{ MPa}\sqrt{\text{m}}$ and $K_{II} = 4.4 \text{ kPa}\sqrt{\text{m}}$ with crack region masked in blue

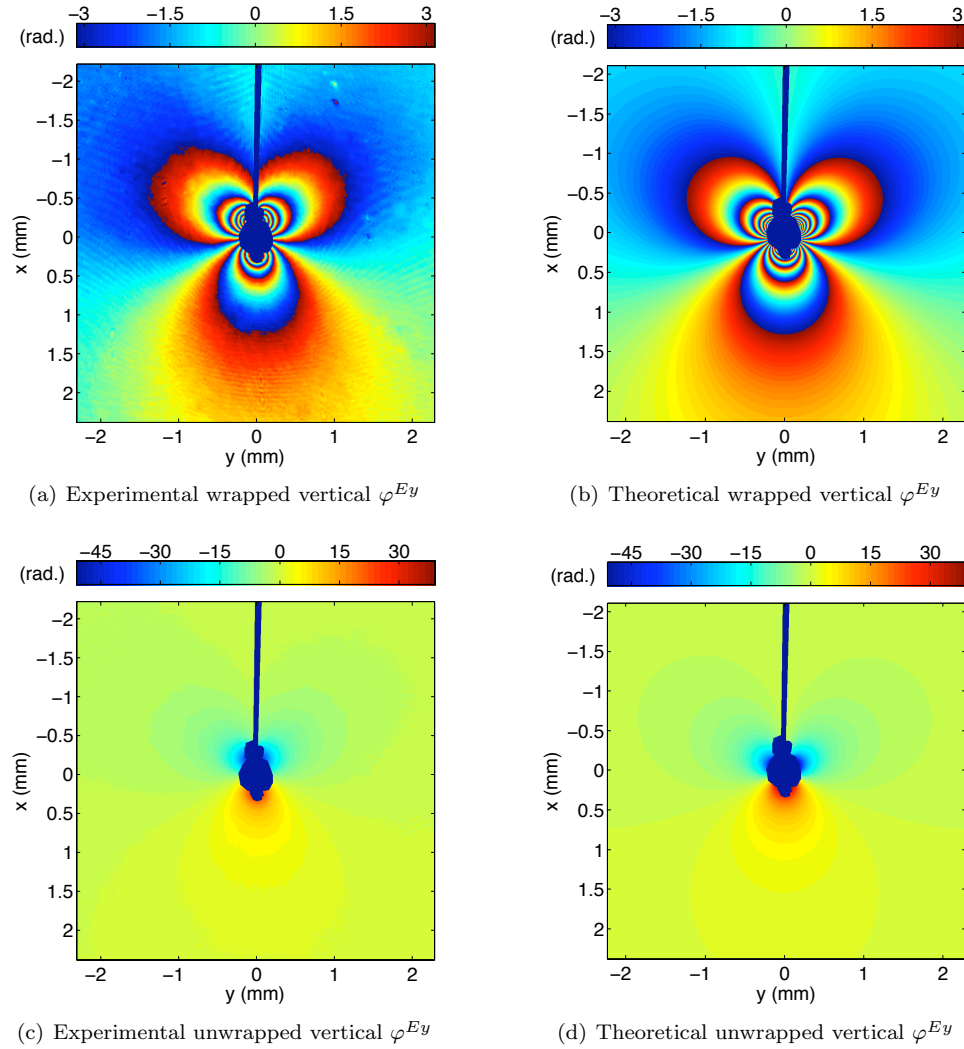


Figure 4.21: Experimental and theoretical φ^{Ey} data for vertical CGS for specimen HomC1 for $K_I = 0.514 \text{ MPa}\sqrt{\text{m}}$ and $K_{II} = 4.4 \text{ kPa}\sqrt{\text{m}}$ with crack region masked in blue

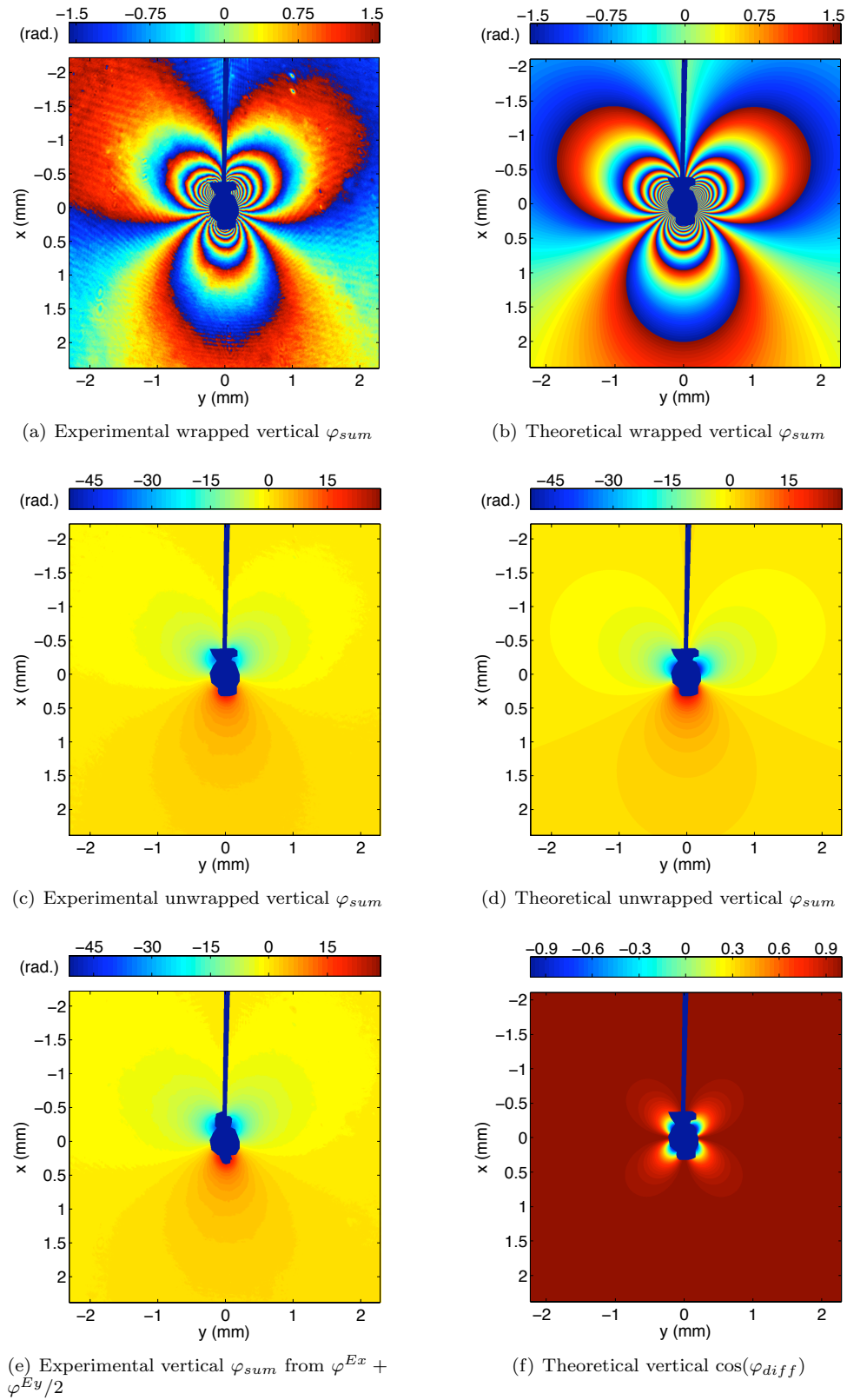


Figure 4.22: Experimental and theoretical φ_{sum} data for vertical CGS from the circularly polarized electric field input data and from the combined pure $E_x\hat{i}$ and $E_y\hat{j}$ data for specimen HomC1 for $K_I = 0.514 \text{ MPa}\sqrt{\text{m}}$ and $K_{II} = 4.4 \text{ kPa}\sqrt{\text{m}}$ with crack region masked in blue

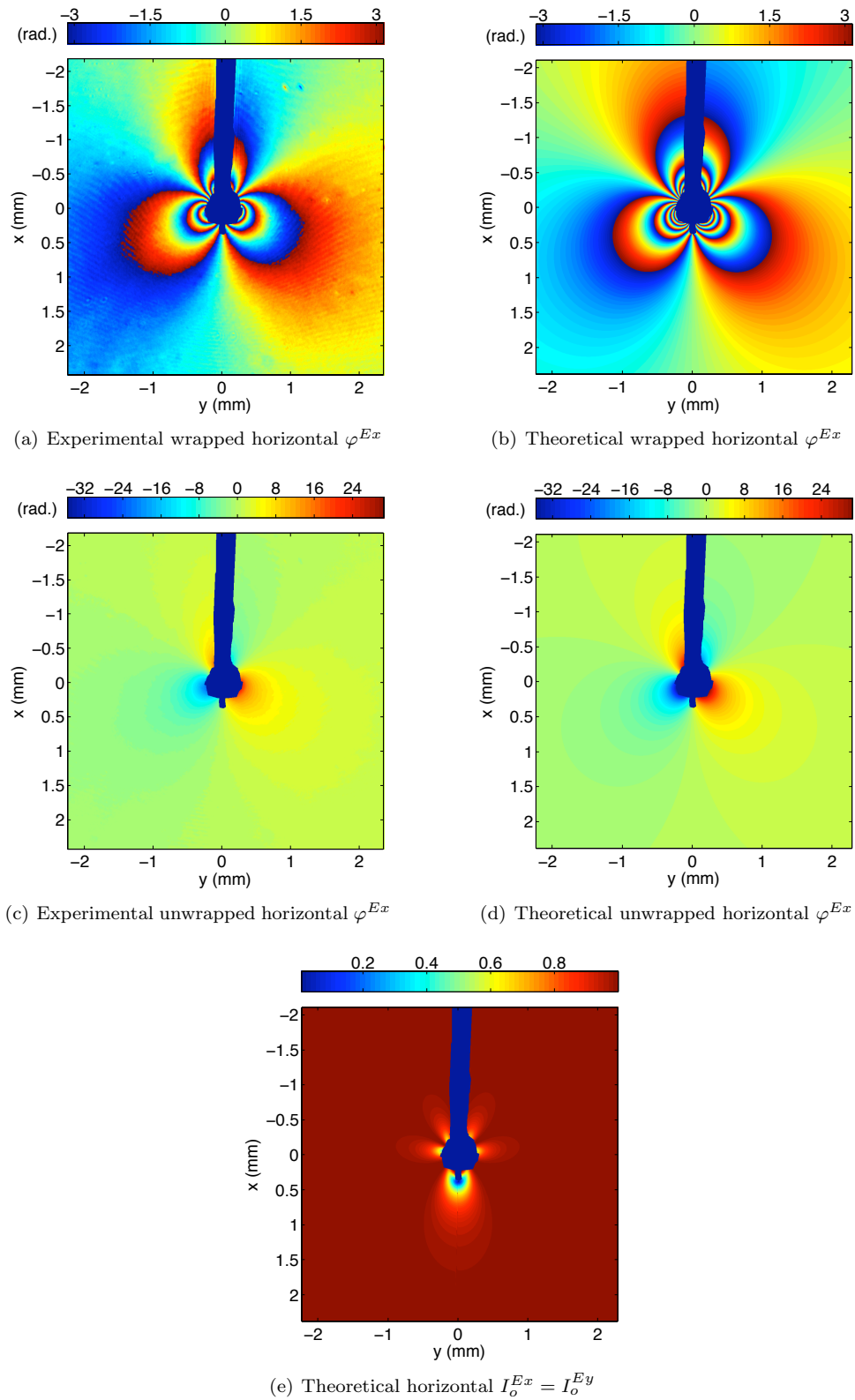


Figure 4.23: Experimental and theoretical φ^{Ex} data for horizontal CGS for specimen HomC1 for $K_I = 0.514 \text{ MPa}\sqrt{\text{m}}$ and $K_{II} = 4.4 \text{ kPa}\sqrt{\text{m}}$ with crack region masked in blue